Exploring mesoscale phenomena in Venusian cloud tops using the scattering transform

Anonymous Author(s)
Affiliation
Address
email

Abstract

This study proposes scattering transform-based quantitative metrics to compare and analyze mesoscale structures (mesoscale; $\sim$1–1,000 km) observed in 365 nm ultraviolet images of the Venusian cloud tops, as well as to identify cloud morphologies and to quantitatively assess the periodicity of mesoscale morphological evolution. We use square regions of interest extracted from Akatsuki Ultraviolet Imager observations on the low-latitude ($5° \leq \lambda_{\text{lat}} \leq 35°$) northern hemisphere afternoon side (12:00–14:00 LT). After applying standard photometric correction and preprocessing to enhance the mesoscale component, we compute scattering transform coefficients and define two metrics, s_{21} and s_{22}, from the first-order and second-order scattering coefficients. The metric s_{21} quantifies the sparsity of morphological features through the relative magnitude of the second-order coefficient (S_2) compared to the first-order coefficient (S_1), whereas s_{22} characterizes the dominant directional anisotropy (i.e., preferred propagation/orientation) through the directional distribution of the second-order coefficient ($S_{2,\parallel}$, $S_{2,\perp}$). In the proposed metric space, mesoscale structures exhibit a tendency to separate by spatial features, demonstrating that images can be systematically explored at targeted features. By tracking the metrics in time, we further identify quasi-periodic variability, suggesting that the proposed framework can simultaneously trace wave-like components associated with the atmospheric super-rotation and mesoscale morphological evolution. The metrics are not intended to directly retrieve physical quantities; rather, they serve as quantitative aids for morphology-based interpretation. Future applications include extending metrics–morphology labeling and performing regional comparisons of occurrence frequency and inter-feature relationships.

1 Introduction

Venus is a so-called twin planet of the Earth due to its similar mass, radius, and distance from the Sun. In remote observations using spacecraft, the major difference between Earth and Venus is the global cloud coverage on Venus, while Earth shows irregular alternations between cloudy and land/sea scenes. The Venus clouds are composed of sulfuric acid, and such a condition could be ubiquitous in exoplanets with active volcanic outgassing, which could be a source of sulfur and water, in the universe.

The cloud-top level of Venus is located around 75 km above the surface. This altitude overlaps with the maximum zonal wind speed that reaches $\sim$100 m/s. This strong zonal wind has been called 'super-rotation'. This super-rotating atmosphere has been one of the big mysteries in the Solar System to explain its origin and maintenance mechanisms, considering the extremely slow rotation period of the planet, 243 Earth days (hereafter, day), implying that the atmospheric rotation is 60 times faster than the planet's rotation (Schubert et al. [2007]). Likely, solar heating near the cloud tops

and atmospheric waves are associated with super-rotation by generating and transferring energy and momentum (Sánchez-Lavega et al. [2017]).

The solar heating is, in particular, noticeable at ultra-violet (UV) and blue wavelength range, due to an unidentified absorber(s) (hereafter, unknown absorber). The unknown absorber produces dynamic cloud morphologies on the planet, and the 365 nm channel has been extensively used in the past spacecraft to track clouds (Horinouchi et al. [2024]). The most recent space mission is the Japanese mission, Akatsuki (2015–2025), which concluded its operation only last year. The UV Imager (UVI) aboard Akatsuki acquired a number of images at 283 and 365 nm, targeting SO_2 gas and the unknown absorber (Yamazaki et al. [2018]). The UVI images reveal complex mesoscale ($\sim$1–1,000 km) structures around the equator, including frequent cellular patterns, linear belts, and wave-like streaks. Previous studies have suggested that these mesoscale phenomena display quasi-periodic oscillations and may be linked to planetary-scale atmospheric dynamics (Kopparla et al. [2019], Kitahara et al. [2019]).

Classifying mesoscale structures and tracking their temporal evolution are essential for understanding the dynamics of the Venusian cloud tops. However, robust quantitative characterization of image-based features remains challenging due to variations in observing conditions (time, illumination, and viewing geometry) as well as the continuous changes in cloud morphology (Suda et al. [2023]). In addition, learning-based classification methods are strongly dependent on training data and labels, and typically require additional design choices to ensure consistent feature representations across changing observational epochs (Mittendorf et al. [2024]). These limitations motivate the need for a methodology that can summarize texture and morphological information without supervised training and express scale-, time-dependent structural differences in continuous, quantitative terms systematically.

To address this need, we propose a quantitative-metric analysis framework based on the scattering transform. The scattering transform summarizes "texture" signals through multiscale wavelet convolutions and nonlinear modulus operations, yielding translation- and rotation-invariant descriptors without data-intensive training. We apply the scattering transform to the mapped UVI dataset and compute scattering transform coefficients. We then define two summary metrics, $s21$ and $s22$, from the relationship between the first- and second-order scattering coefficients. The metric $s21$ is designed to quantify the sparsity of morphological features via the relative magnitude of the second-order component compared to the first-order component, whereas $s22$ captures the dominant directional anisotropy (preferred propagation/orientation) through the directional distribution of the second-order component.

For example, we show that distinct mesoscale morphologies at different spatial scales tend to separate in the metric space. This enables systematic exploration of image supporting morphology-based classification and visual inspection. Moreover, by tracking metric variations over time, we can identify quasi-periodic variability and morphological evolution of mesoscale phenomena. We note that the proposed metrics are intended not as direct retrievals of physical quantities, but as quantitative aids for morphology-based interpretation. Our proposed method will allow us to explore further wave-based explanations to better understand the mechanisms that maintain the super-rotation. Our proposed method will scientific contributions to the upcoming future Venus missions by Europe and USA, ESA's EnVision (Wilson and Widemann [2016]) and NASA's DAVINCI (Garvin et al. [2022]), while Korea already takes part in ESA's EnVision as a co-investigator (Institute for Basic Science [2024]).

2 Data

Akatsuki spacecraft has been on an elliptic equatorial orbit around Venus since December 2015, with an orbital period of approximately 10.5 days. The onboard UV Imager (UVI) acquires images in two bands centered at 283 nm and 365 nm. The former is strongly affected by SO_2 absorption, whereas the latter is largely influenced by an unknown absorber. In this study, we focus exclusively on the 365 nm ultraviolet images. We use the Level-3b (L3b) data product in which the raw disk images are mapped onto a latitude–longitude grid assuming a spherical Venus (Ogohara et al. [2017]). The data are provided as netCDF files and include metadata such as latitude, longitude, local time, phase angle, incidence angle, emission angle. Our analysis covers observations from May 2016 to June 2022. After outlier screening, a total of 2,558 images are retained and used in the subsequent analyses.

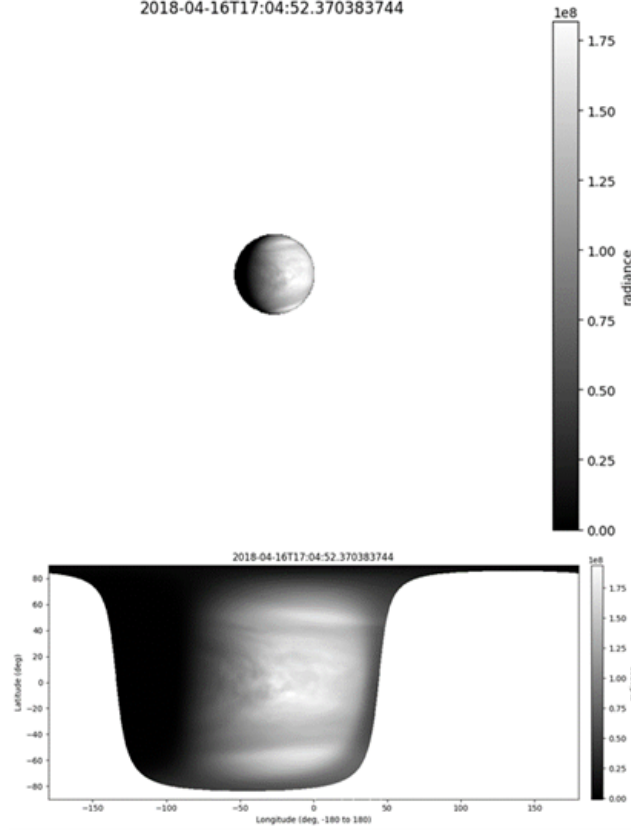Figure 1: 2018-04-16. Venus images acquired at the same time (top: L3bx; bottom: L3b).
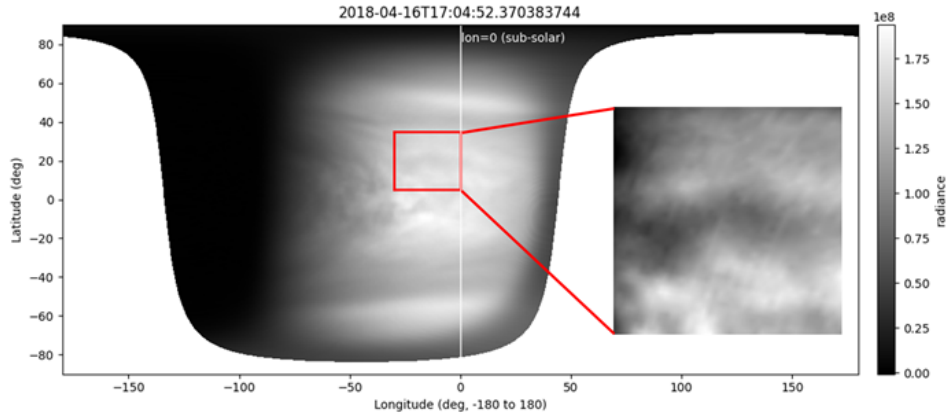
2.1 Target area of the application

Figure 2: Region of interest (ROI) overlaid on the Venus image.

To analyze mesoscale phenomena in the low-latitude northern hemisphere of Venus, we define a region of interest (ROI) and apply preprocessing within this domain. To align longitudes with respect to the sub-solar point, we introduce the relative longitude as

$$\lambda_{\mathrm{lon,rel}} = (\lambda_{\mathrm{lon}} - \lambda_{\mathrm{lon,sun}} + 180°) \mod 360° + 180°$$

where $\lambda_{\mathrm{lon,sun}}$ denotes the sub-solar longitude. The ROI is then extracted over $5° \leq \lambda_{\mathrm{lat}} \leq 35°$ in latitude and $-30° \leq \lambda_{\mathrm{lon,rel}} \leq 0°$ in relative longitude (12:00–14:00 LT). To ensure a comparable

3

effective spatial resolution across the dataset, we exclude observations acquired when the Venus–spacecraft distance (ranging from $\sim 10{,}000$ to $\sim 370{,}000$ km) exceeds a prescribed threshold; specifically, files with distances less than 306,121.8 km are removed from the analysis.

2.2 Pre-processing and Standardization

To obtain quality-controlled scenes, we first discard pixels for which the radiance or viewing-geometry variables (e.g., incidence angle and emission angle) are non-finite. The excluded pixels are masked as missing values (NaN). In addition, scenes are removed from the analysis if NaN values remain within the ROI. We applied a Minnaert law for the photometric correction (Minnaert [1941]). To further suppress strong limb effects, we mask pixels whose incidence angle and emission angle are both exceed a threshold angle $\alpha = 75°$.

To remove residual extreme values that may persist after photometric correction, we apply outlier filtering based on the median and the median absolute deviation (MAD). After extracting the ROI, we perform a center-crop to obtain a square domain when the ROI is near-square (originally rectangular). To prevent artificial signals introduced by missing data, we discard the entire scene if any NaN/Inf values remain within the ROI after masking and outlier removal.

Table 1: Summary of the dataset used in the analysis

	Usable data	
Index	Period (YYYY-MM-DD)	Number of selected images
1	2016-05-03 $\sim$ 2016-05-25	18
2	2016-06-23 $\sim$ 2016-07-07	78
3	2016-12-08 $\sim$ 2017-02-13	234
4	2017-07-16 $\sim$ 2017-09-21	316
5	2018-02-21 $\sim$ 2018-05-07	283
6	2018-09-29 $\sim$ 2018-12-13	333
7	2019-05-14 $\sim$ 2019-07-20	280
8	2019-12-29 $\sim$ 2020-02-25	268
9	2020-07-28 $\sim$ 2020-09-30	190
10	2021-03-06 $\sim$ 2021-03-17	43
11	2021-04-08 $\sim$ 2021-05-11	152
12	2021-10-13 $\sim$ 2021-12-18	292
13	2022-05-22 $\sim$ 2022-06-05	71

To standardize the inputs in both spatial and statistical senses, we apply high-pass flattening and normalization. For an ROI image X, we first compute a gaussian-blurred field $G_{\sigma_f}(X)$ ($\sigma_f = 32$) and then obtain a flattened image that emphasizes mesoscale components,

$$X_{\text{flat}} = X - G_{\sigma_f}(X).$$

We next perform z-score normalization using the mean and standard deviation of X_{flat}, multiply the result by a scaling factor ($c_s = 0.33$), and clip the values to the range $[-1, 1]$. Finally, to enforce a uniform spatial resolution across the dataset, all inputs are resized to 256×256 using linear interpolation (order = 1).
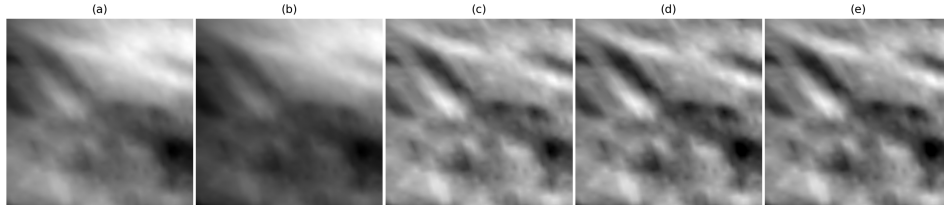

Figure 3: Example showing the image evolution through the preprocessing steps: (a) raw image, (b) after applying photometric correction, (c) after flattening, (d) after normalization, and (e) the final image.
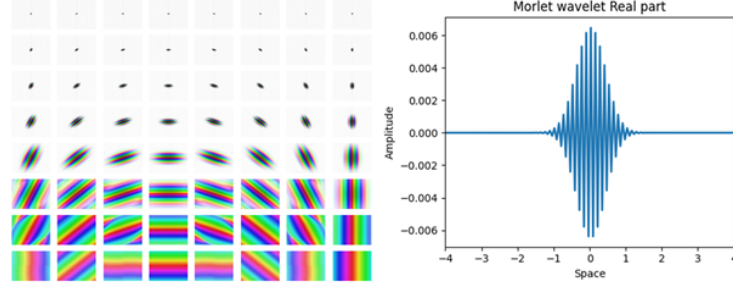
3 Method: Scattering Transform

Figure 4: Morlet wavelet filter morphology.

The scattering transform was proposed by Mallat and applied to observational cosmology by Cheng (Mallat [2012], Cheng et al. [2020]). The scattering transform summarizes image "texture" signals through multiscale, multi-orientation convolutions and nonlinear modulus operations, providing translation- and rotation-invariant descriptors. We calculate these descriptors to quantify directional and sparse components of cloud morphologies, in contrast to deep learning-based feature extractors. While the orders of scattering coefficients imply increasing levels of statistical complexity, the 0th-, 1st-, and 2nd-order scattering coefficients are defined as

$$S_0 \equiv \langle I_0 * \phi_J \rangle$$

$$S_{1,j_1}(j_1) \equiv \langle I_1^{(j_1)} * \phi_J \rangle_{l_1} = \langle |I_0 * \psi^{(j_1)}| * \phi_J \rangle_{l_1}$$

$$S_2(j_1, j_2) \equiv \langle I_2^{(j_1,j_2)} * \phi_J \rangle_{l_1 j_2 l_2} = \langle ||I_0 * \psi^{(j_1)}| * \psi^{(j_2)}| * \phi_J \rangle_{l_1 j_2 l_2},$$

where I_0 denotes the input image, ψ is a family of complex wavelets, ϕ_J is a low-pass averaging filter at scale J, $*$ denotes convolution, and $\langle \cdot \rangle$ indicates spatial averaging. The intermediate fields I_1 and I_2 correspond to the first- and second-order scattering fields, obtained by successive applications of wavelet convolution and modulus operations to the input image.

We apply the Kymatio-based 2D scattering transform to the preprocessed 256×256 single-channel images (Andreux et al. [2020]). We use morlet wavelets with $J = 8$, corresponding to eight dyadic scales ($2^j, j = 0, 1, \ldots, 7$), and employ eight orientations to compute orientation-averaged statistics. The maximum scattering order is set to 2. Each scattering coefficient map is spatially averaged, yielding a scalar coefficient for each scattering path. In the subsequent analysis, we exclude the zeroth-order coefficients and compute the following two metrics using only the first- and second-order coefficients.

3.1 Definition of scattering transform-based summary statistics and spatially resolved metrics

Cheng and Ménard [2021] formulated scattering coefficients in the context of stationary ergodic textures, where the spatial average computed from a single realization is interpreted as an approximation to the ensemble average; accordingly, they used globally averaged scattering coefficients S_1 and S_2. However, the Venus cloud images analyzed in this study do not satisfy global stationarity and ergodicity. Therefore, although we compute s_{21} and s_{22} using the same ratio-based definitions, we interpret them as empirical summary descriptors for comparative feature analysis rather than as ensemble-based texture measures. In addition, we retain the scale dependence by reporting $s_{21}(j_1)$ and $s_{22}(j_1)$ for each j_1, while averaging over scattering paths and orientations as in Cheng and Ménard [2021].

3.2 Normalized second-to-first order ratio: s21

The metric s_{21} quantifies the sparsity of morphological features through the relative magnitude of the second-order scattering coefficient compared to the first-order coefficient. For a given scale j_1, we

5

average the ratio over all second-order scattering paths with $j_2 > j_1$ and over all combinations of orientations, and define

$$s_{21}^{\mathrm{RoA}}(j_1) = \left\langle \frac{S_2(j_1, l_1, j_2, l_2)}{S_1(j_1, l_1)} \right\rangle_{(j_2, l_1, l_2)}.$$

Due to the constraint $j_2 > j_1$, in this study, we compute s_{21} for $j_1 = 0$–6, corresponding to spatial scales of approximately 12.5–801.3 km.

3.3 Ratio of parallel to orthogonal directional components: s22

The metric s_{22} characterizes the dominant directional anisotropy (preferred propagation/orientation) through the directional distribution of the second-order scattering component. For a given scale pair (j_1, j_2), we construct two second-order paths based on the relative orientation between the two wavelet convolutions: a parallel configuration with $l_2 = l_1$ and an orthogonal configuration with $l_2 = l_1 + L/2$, where L is the number of orientations. We then define

$$s_{22}^{\mathrm{RoA}}(j_1) = \left\langle \frac{S_2(j_1, l_1, j_2, l_{2,\parallel})}{S_2(j_1, l_1, j_2, l_{2,\perp})} \right\rangle_{(j_2, l_1)}.$$

Here, $l_{2,\parallel}$ and $l_{2,\perp}$ denote the orientations corresponding to the parallel and orthogonal cases, respectively.

3.4 Scatter plot

Using s_{21} and s_{22} derived from the scattering transform for each image, we examine the distribution of Venusian cloud tops morphologies in the (s_{21}, s_{22}) space as a function of the first-order wavelet scale j_1.
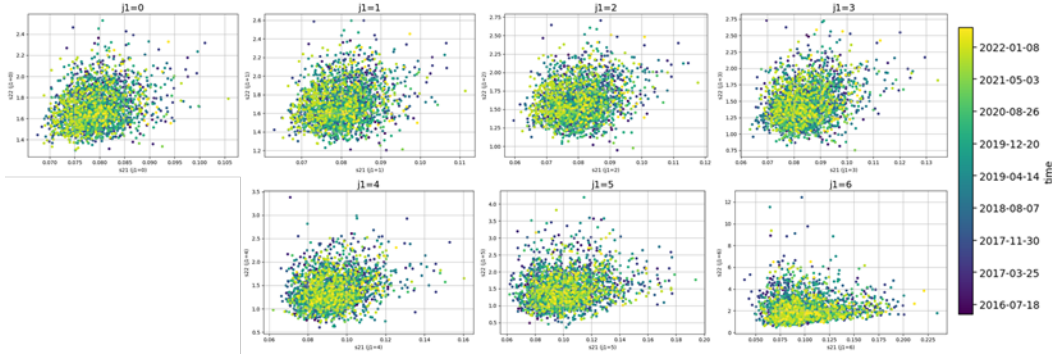

Figure 5: Scatter plots of s_{21} (x-axis) versus s_{22} (y-axis) for $j_1 = 0$–6.

We plot the (s_{21}, s_{22}) placement of the full dataset. The samples are distributed broadly within the same domain without an obvious long-term drift, indicating that the mesoscale morphology oscillates within bounded limits over the full-time span (~ 6 years). We also find that the spread (standard deviation) of the population distribution increases with increasing j_1. This can be interpreted as a reduction in robustness at larger j_1, because only paths satisfying $j_2 > j_1$ contribute to the next-order statistics; as j_1 increases, fewer admissible j_2 values remain to be averaged, thereby reducing the effective sample size in the averaging and increasing variability.

4 Results

4.1 Image Map

By replacing each point in the scatter plot with a representative image, we obtain an "image map" over the (s_{21}, s_{22}) plane. Comparison with visual inspection suggests that morphological separation is most effective for $j_1 = 3, 4, 5$. For $j_1 = 0, 1, 2$, the corresponding structures reflect scales of 1, 2, and 4 pixels, respectively, and thus emphasize highly local features. In contrast, the mesoscale

structures of interest are more clearly expressed at 8-, 16-, and 32-pixel scales, which aligns with the improved separation observed for $j_1 = 3, 4, 5$. For $j_1 = 6$, the scale corresponds to 64 pixels; however, the robustness decreases, and the resulting separation becomes less reliable.
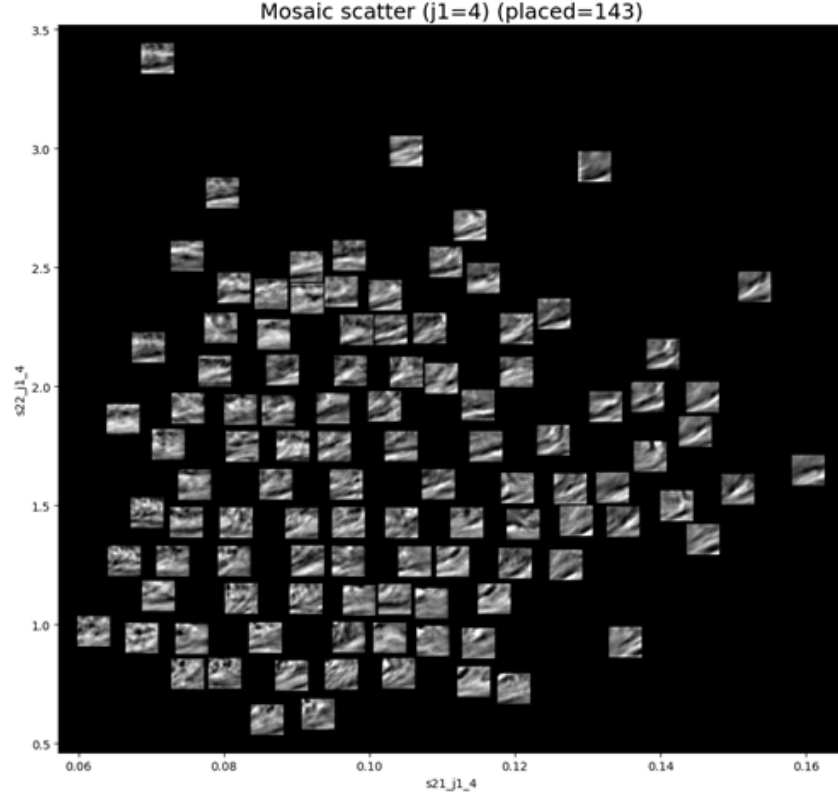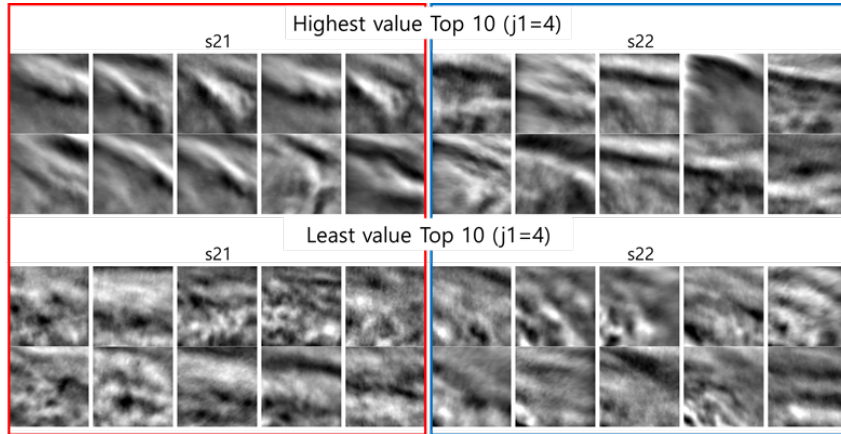

Figure 6: Image maps at $j_1 = 4$.

Figure 7: Detailed image map at $j_1 = 4$; top 10 and bottom 10 samples by s_{21} (upper-left and lower-left panels, respectively), and top 10 and bottom 10 samples by s_{22} (upper-right and lower-right panels, respectively).

Focusing on the image map at $j_1 = 4$, we find that convective-like cell patterns are prominent when s_{21} is small, whereas cellular structures become less evident and the UV absorber appears more concentrated in linear features when s_{21} is large. For s_{22}, small values are associated with curled or swirling cloud morphologies, whereas large values correspond to more line-like, filamentary structures.
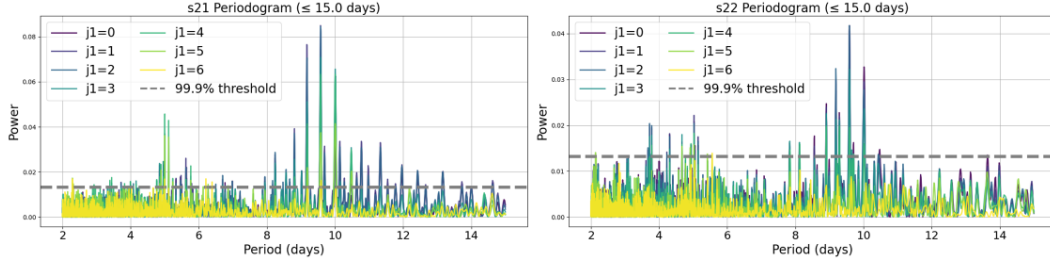
7

4.2 Quasi-periodic Variability

Figure 8: Lomb–Scargle periodograms for $j_1 = 0$–6 with the 99.9% significance threshold.

When examining the temporal evolution of s_{21} and s_{22} as a function of j_1, we identify quasi-periodic oscillations. To quantify the dominant periods, we perform Lomb–Scargle periodogram analysis over the 2–15 days range. As a result, a periodicity near ~ 9.5 days is detected in both s_{21} and s_{22}. For s_{21}, an additional enhancement of variability near ~ 5 days is evident for $j_1 = 3, 4, 5$. For s_{22}, a ~ 5 day periodicity is also detected ($j_1 = 1, 2, 3, 4, 5$), and a further peak near ~ 3.9 days is emphasized for $j_1 = 1, 2, 3, 4$.

The averaged zonal wind speed (super-rotation) during the sampled data period (May 2016 to June 2022), at low latitudes is approximately 84–$96\ \mathrm{m\,s^{-1}}$ at $365\ \mathrm{nm}$ (Horinouchi et al. [2024]). This corresponds to an atmospheric rotation period of about ~ 4.4–5.0 days, representing the background wind advection. Superposed on this background flow, we identify atmospheric wave activities with distinct periodicities: a ~ 5 days signal propagating more slowly than the zonal winds, consistent with Rossby waves, and a ~ 3.9 days signal propagating faster than the zonal winds, consistent with Kelvin waves. In addition, a ~ 9.5 days periodicity is attributed to phase-angle-dependent UV contrast associated with the spacecraft orbital cycle. We further hypothesize that the confinement of the ~ 3.9-day periodicity to s_{22} reflects the fact that low-latitude Kelvin-wave signatures can manifest as fast-propagating disturbances embedded in high-speed streams, with phase speeds exceeding those of the background super-rotating zonal flow. Such disturbances can produce fine, anisotropic UV-contrast pattern, which are preferentially captured by second-order scattering statistics.

5 Conclusions

In this study, we propose scattering-transform-based quantitative metrics, s_{21} and s_{22}, tailored for Venusian cloud-morphology analysis, to investigate mesoscale structures observed in Akatsuki UVI $365\ \mathrm{nm}$ cloud-top images to identify cloud morphologies and to quantitatively assess the periodicity of mesoscale morphological evolution. After applying standard photometric correction and preprocessing designed to enhance the mesoscale component, we compute scattering coefficients and define a sparsity metric (s_{21}) and a directional-anisotropy metric (s_{22}). This yields a stable coordinate system that summarizes image morphology without supervised training, in contrast to CNN-based approaches that often face challenges in mesoscale pattern classification.(Mittendorf et al. [2024])

Within the proposed metric space, mesoscale structures show a tendency to separate by spatial features. In particular, morphological decomposition is comparatively clear for $j_1 = 3, 4, 5$, supporting the effectiveness of the approach. Furthermore, tracking the temporal evolution of s_{21} and s_{22} and applying Lomb–Scargle analysis reveal quasi-periodic components near 3.9 and 5 days, together with a component near 9.5 days. These results suggest that the proposed metrics can simultaneously trace wave-related variability and morphological evolution in the super-rotating regime.

Importantly, the proposed metrics are intended not to directly retrieve physical quantities, but to serve as quantitative support for morphology-based interpretation. Specifically, by selecting area of interest in the (s_{21}, s_{22}) space and inspecting representative images, one can systematically collect and compare targeted morphologies from large image archives, reduce the subjectivity inherent in manual inspection, and efficiently identify events associated with quasi-periodic variability. In this sense, the framework provides a scalable and reproducible analysis pathway for high-volume

image datasets, which can help support upcoming Venus missions by enabling systematic, consistent morphology screening and event selection across large archives.

We note several limitations. First, the present analysis focuses on a restricted observational domain (currently limited to low-latitude regions and a specific local-time sector), and the resulting metric distributions and periodicities may not directly generalize to other latitudes or local times without further validation. Second, morphological separation is not equally robust across all spatial scales: the decomposition is most distinct for $j_1 = 3$–5, whereas classification becomes less clear at the smallest scales ($j_1 = 0$–2) and at the largest scale considered ($j_1 = 6$). Future work will extend morphology labeling in the metric space and apply regional and local-time comparisons of index distributions, together with wave-period diagnostics, to further constrain the atmospheric dynamics of the Venusian cloud tops.

References

Mathieu Andreux, Tomas Angles, Georgios Exarchakis, Roberto Leonarduzzi, Gaspar Rochette, Louis Thiry, John Zarka, Stephane Mallat, Joakim Anden, Eugene Belilovsky, Joan Bruna, Vincent Lostanlen, Muawiz Chaudhary, Matthew J. Hirn, Edouard Oyallon, Sixin Zhang, Carmine Cella, and Michael Eickenberg. Kymatio: Scattering transforms in python. *Journal of Machine Learning Research*, 21(60):1–6, 2020. URL http://jmlr.org/papers/v21/19-047.html.

Sihao Cheng and Brice Ménard. How to quantify fields or textures? A guide to the scattering transform, November 2021. URL http://arxiv.org/abs/2112.01288. arXiv:2112.01288 [astro-ph].

Sihao Cheng, Yuan-Sen Ting, Brice Ménard, and Joan Bruna. A new approach to observational cosmology using the scattering transform. *Monthly Notices of the Royal Astronomical Society*, 499(4):5902–5914, November 2020. ISSN 0035-8711, 1365-2966. doi: 10.1093/mnras/staa3165. URL https://academic.oup.com/mnras/article/499/4/5902/5924461.

James B. Garvin, Stephanie A. Getty, Giada N. Arney, Natasha M. Johnson, Erika Kohler, Kenneth O. Schwer, Michael Sekerak, Arlin Bartels, Richard S. Saylor, Vincent E. Elliott, Colby S. Goodloe, Matthew B. Garrison, Valeria Cottini, Noam Izenberg, Ralph Lorenz, Charles A. Malespin, Michael Ravine, Christopher R. Webster, David H. Atkinson, Shahid Aslam, Sushil Atreya, Brent J. Bos, William B. Brinckerhoff, Bruce Campbell, David Crisp, Justin R. Filiberto, Francois Forget, Martha Gilmore, Nicolas Gorius, David Grinspoon, Amy E. Hofmann, Stephen R. Kane, Walter Kiefer, Sebastien Lebonnois, Paul R. Mahaffy, Alexander Pavlov, Melissa Trainer, Kevin J. Zahnle, and Mikhail Zolotov. Revealing the Mysteries of Venus: The DAVINCI Mission. *The Planetary Science Journal*, 3(5):117, May 2022. ISSN 2632-3338. doi: 10.3847/PSJ/ac63c2. URL https://iopscience.iop.org/article/10.3847/PSJ/ac63c2.

Takeshi Horinouchi, Toru Kouyama, Masataka Imai, Shin-ya Murakami, Yeon Joo Lee, Atsushi Yamazaki, Manabu Yamada, Shigeto Watanabe, Takeshi Imamura, Javier Peralta, and Takehiko Satoh. Long-Term Variability of Mean Winds and Planetary-Scale Waves Around Venusian Cloud Top Observed With Akatsuki/UVI. *Journal of Geophysical Research (Planets)*, 129(3): e2023JE008221, March 2024. doi: 10.1029/2023JE008221.

Institute for Basic Science. South korean researcher joins esa envision venus mission as co-investigator. https://www.ibs.re.kr/cop/bbs/BBSMSTR_000000000739/selectBoardArticle.do?nttId=24858, 2024. Press release.

Takehiko Kitahara, Takeshi Imamura, Takao M. Sato, Atsushi Yamazaki, Yeon Joo Lee, Manabu Yamada, Shigeto Watanabe, Makoto Taguchi, Tetsuya Fukuhara, Toru Kouyama, Shin-ya Murakami, George L. Hashimoto, Kazunori Ogohara, Hiroki Kashimura, Takeshi Horinouchi, and Masahiro Takagi. Stationary Features at the Cloud Top of Venus Observed by Ultraviolet Imager Onboard Akatsuki. *Journal of Geophysical Research (Planets)*, 124(5):1266–1281, May 2019. doi: 10.1029/2018JE005842.

Pushkar Kopparla, Yeon Joo Lee, Takeshi Imamura, and Atsushi Yamazaki. Principal components of short-term variability in the ultraviolet albedo of venus. *Astron. Astrophys.*, 626:A30, 2019. doi: 10.1051/0004-6361/201935388. URL https://doi.org/10.1051/0004-6361/201935388.

Stéphane Mallat. Group Invariant Scattering. *Communications on Pure and Applied Mathematics*, 65(10):1331–1398, October 2012. ISSN 0010-3640, 1097-0312. doi: 10.1002/cpa.21413. URL `https://onlinelibrary.wiley.com/doi/10.1002/cpa.21413`.

M. Minnaert. The reciprocity principle in lunar photometry. , 93:403–410, May 1941. doi: 10.1086/144279.

J. Mittendorf, K. Molaverdikhani, B. Ercolano, A. Giovagnoli, and T. Grassi. Classifying the clouds of Venus using unsupervised machine learning. *Astronomy and Computing*, 49:100884, October 2024. ISSN 22131337. doi: 10.1016/j.ascom.2024.100884. URL `https://linkinghub.elsevier.com/retrieve/pii/S2213133724000994`.

Kazunori Ogohara, Masahiro Takagi, Shin-ya Murakami, Takeshi Horinouchi, Manabu Yamada, Toru Kouyama, George L. Hashimoto, Takeshi Imamura, Yukio Yamamoto, Hiroki Kashimura, Naru Hirata, Naoki Sato, Atsushi Yamazaki, Takehiko Satoh, Naomoto Iwagami, Makoto Taguchi, Shigeto Watanabe, Takao M. Sato, Shoko Ohtsuki, Tetsuya Fukuhara, Masahiko Futaguchi, Takeshi Sakanoi, Shingo Kameda, Ko-ichiro Sugiyama, Hiroki Ando, Yeon Joo Lee, Masato Nakamura, Makoto Suzuki, Chikako Hirose, Nobuaki Ishii, and Takumi Abe. Overview of Akatsuki data products: definition of data levels, method and accuracy of geometric correction. *Earth, Planets and Space*, 69(1):167, December 2017. ISSN 1880-5981. doi: 10.1186/s40623-017-0749-5. URL `https://earth-planets-space.springeropen.com/articles/10.1186/s40623-017-0749-5`.

Agustín Sánchez-Lavega, Sebastien Lebonnois, Takeshi Imamura, Peter Read, and David Luz. The Atmospheric Dynamics of Venus. , 212(3-4):1541–1616, November 2017. doi: 10.1007/s11214-017-0389-x.

G. Schubert, S. W. Bougher, C. C. Covey, A. D. Del Genio, J. L. Grossman, A. S.and Hollingsworth, S. S. Limaye, and R. E. Young. Venus atmosphere dynamics: A continuing enigma. In L. Esposito, E. R. Stofan, and T. E. Cravens, editors, *Exploring Venus as a terrestrial planet*, Geophysical monograph series, pages 101–120. American Geophysical Union, 2007. ISBN 9780875904412. URL `http://books.google.de/books?id=YZ8RAQAAIAAJ`.

Tomoya Suda, Takeshi Imamura, Yeon Joo Lee, Atsushi Yamazaki, Takehiko Satoh, and Takao M. Sato. Periodic Variation of Mesoscale Ultraviolet Contrast at the Cloud Top of Venus. *Journal of Geophysical Research: Planets*, 128(10):e2023JE007852, 2023. ISSN 2169-9100. doi: 10.1029/2023JE007852. URL `https://onlinelibrary.wiley.com/doi/abs/10.1029/2023JE007852`. _eprint: https://onlinelibrary.wiley.com/doi/pdf/10.1029/2023JE007852.

F Wilson and T Widemann. ENVISION M5 VENUS ORBITER PROPOSAL: OPPORTUNITIES AND CHALLENGES. R. C. Ghail1, C. 2016.

Atsushi Yamazaki, Manabu Yamada, Yeon Joo Lee, Shigeto Watanabe, Takeshi Horinouchi, Shin-ya Murakami, Toru Kouyama, Kazunori Ogohara, Takeshi Imamura, Takao M. Sato, Yukio Yamamoto, Tetsuya Fukuhara, Hiroki Ando, Ko-ichiro Sugiyama, Seiko Takagi, Hiroki Kashimura, Shoko Ohtsuki, Naru Hirata, George L. Hashimoto, Makoto Suzuki, Chikako Hirose, Munetaka Ueno, Takehiko Satoh, Takumi Abe, Nobuaki Ishii, and Masato Nakamura. Ultraviolet imager on venus orbiter akatsuki and its initial results. *Earth, Planets and Space*, 70(1):23, Feb 2018. ISSN 1880-5981. doi: 10.1186/s40623-017-0772-6. URL `https://doi.org/10.1186/s40623-017-0772-6`.

A Appendix

A.1 Compute Resources

Compute resources (CPU-only). All experiments were run in a Jupyter Notebook (ipynb) using Python 3.13.1 on a CPU-only system with Intel® Core™ Ultra 5 135U (12 cores / 14 threads, base 2.10 GHz) and 15.5 GB RAM; no GPU/NPU acceleration was used. Preprocessing 15,107 files took $\sim$ 20h, and applying the scattering transform took $\sim$ 1h 15min on this system.

A.2 Licenses for existing assets

We used Akatsuki/UVI Level-3b (365 nm) data distributed via JAXA/ISAS DARTS under CC BY 4.0. We computed scattering coefficients with Kymatio, licensed under BSD-3-Clause. All codes used this study have been anonymized and are attached as a ZIP file.

A.3 Open access to data & code

All data are available as open data from the Akatsuki Science Data Archive, and all codes have been anonymized and are attached as a ZIP file.
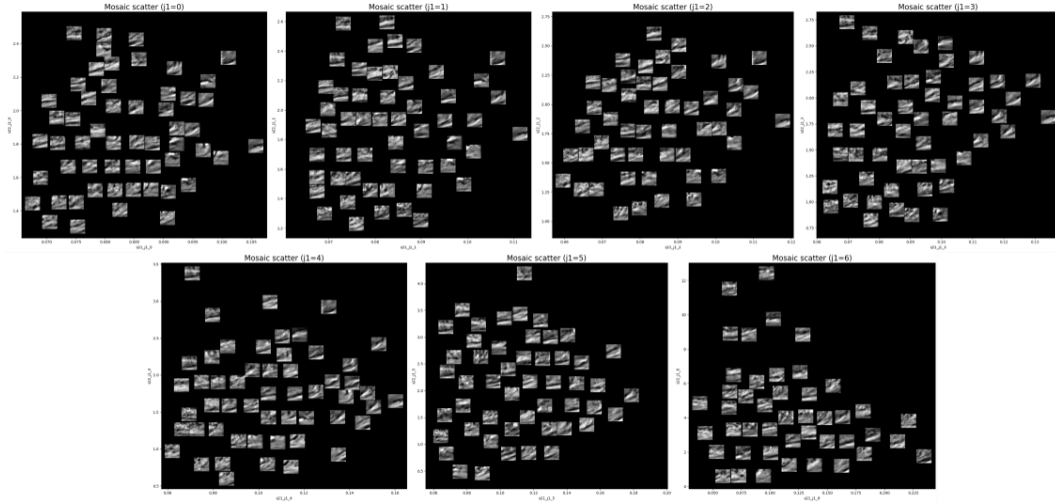
A.4 Image map

Figure 9: Image maps at $j_1 = 0 - 6$.

11

AI Co-Scientist Challenge Korea Paper Checklist

1. **Claims**

   Question: Do the main claims made in the abstract and introduction accurately reflect the paper's contributions and scope?

   Answer: [Yes]

   Justification: The core contributions stated in the abstract/introduction (defining scattering transform-based metrics s21/s22 and using them to separate structures across scales/time and identify quasi-periodicity) are consistently supported in the results and conclusion.

2. **Limitations**

   Question: Does the paper discuss the limitations of the work performed by the authors?

   Answer: [Yes]

   Justification: The conclusion explicitly discusses limitations such as restricted applicability (low latitudes/specific local-time ranges) and unclear separability at certain scales (e.g., $j_1=0$ – 2 and 6).

3. **Theory Assumptions and Proofs**

   Question: For each theoretical result, does the paper provide the full set of assumptions and a complete (and correct) proof?

   Answer: [N/A]

   Justification: The paper is primarily experimental/analytical (definitions + empirical analysis) rather than presenting formal theorems with proofs.

4. **Experimental Result Reproducibility**

   Question: Does the paper fully disclose all the information needed to reproduce the main experimental results of the paper to the extent that it affects the main claims and/or conclusions of the paper (regardless of whether the code and data are provided or not)?

   Answer: [Yes]

   Justification: It provides detailed data coverage (2016 – 2022, 2,558 images), ROI definition, preprocessing (angular masking, MAD-based outlier removal, high-pass flattening/normalization, 256×256 resize), and key configuration details.

5. **Open access to data and code**

   Question: Does the paper provide open access to the data and code, with sufficient instructions to faithfully reproduce the main experimental results, as described in supplemental material?

   Answer: [Yes]

   Justification: The Akatsuki dataset is described as publicly available, and the code is stated to be attached in anonymized ZIP form.

6. **Experimental Setting/Details**

   Question: Does the paper specify all the training and test details (e.g., data splits, hyper-parameters, how they were chosen, type of optimizer, etc.) necessary to understand the results?

   Answer: [Yes]

   Justification: The scattering transform setup (e.g., J=8, 8 orientations, max order=2), the s21/s22 definitions, and the analysis workflow (scale maps, time series and periodicity analysis) are specified.

7. **Experiment Statistical Significance**

   Question: Does the paper report error bars suitably and correctly defined or other appropriate information about the statistical significance of the experiments?

   Answer: [Yes]

   Justification: Lomb–Scargle periodogram results are reported with a 99.9% significance threshold, and key peaks (9.5, 5, 3.9 days) are interpreted.

8. **Experiments Compute Resources**

   Question: For each experiment, does the paper provide sufficient information on the computer resources (type of compute workers, memory, time of execution) needed to reproduce the experiments?

   Answer: [Yes]

   Justification: Appendix A.1 reports CPU/RAM specs, environment (Python 3.13.1, Jupyter), and approximate runtimes for preprocessing and scattering computations.

9. **Code Of Ethics**

   Question: Does the research conducted in the paper conform, in every respect, with the NeurIPS Code of Ethics `https://nips.cc/public/EthicsGuidelines`?

   Answer: [Yes]

   Justification: The work uses publicly available planetary observation data and does not involve human subjects or sensitive personal data; it also includes standard transparency items (e.g., no competing interests/funding statements).

10. **Broader Impacts**

    Question: Does the paper discuss both potential positive societal impacts and negative societal impacts of the work performed?

    Answer: [N/A]

    Justification: This work is a foundational quantitative analysis methodology for Venus atmospheric/mission science products, with no direct path to societal deployment or large-scale negative societal impacts. Its primary impact is scientific and mission-oriented by enabling scalable, reproducible morphology screening and event selection over large image archives, it can support upcoming Venus missions (e.g., ESA's EnVision and NASA's DAVINCI) as highlighted in the Introduction.

11. **Safeguards**

    Question: Does the paper describe safeguards that have been put in place for responsible release of data or models that have a high risk for misuse (e.g., pretrained language models, image generators, or scraped datasets)?

    Answer: [N/A]

    Justification: The study does not introduce a high-misuse-risk model/system (e.g., a deployment-ready generative system or sensitive data pipeline), so explicit safeguards are not central.

12. **Licenses for existing assets**

    Question: Are the creators or original owners of assets (e.g., code, data, models), used in the paper, properly credited and are the license and terms of use explicitly mentioned and properly respected?

    Answer: [Yes]

    Justification: The paper states licenses for key assets (e.g., data under CC BY 4.0 and the Kymatio library under BSD-3-Clause) and credits sources.

13. **New Assets**

    Question: Are new assets introduced in the paper well documented and is the documentation provided alongside the assets?

    Answer: [Yes]

    Justification: This paper provides an anonymized code ZIP as a new asset in the supplementary materials, and also documents the execution environment and compute resources (A.1), data access (A.3), and relevant licenses (A.2), thereby supplying the context needed for reuse.

14. **Crowdsourcing and Research with Human Subjects**

    Question: For crowdsourcing experiments and research with human subjects, does the paper include the full text of instructions given to participants and screenshots, if applicable, as well as details about compensation (if any)?

Answer: [N/A]

Justification: There is no crowdsourcing component (no recruited annotators/participants, compensation, or quality-control protocol).

15. **Institutional Review Board (IRB) Approvals or Equivalent for Research with Human Subjects**

Question: Does the paper describe potential risks incurred by study participants, whether such risks were disclosed to the subjects, and whether Institutional Review Board (IRB) approvals (or an equivalent approval/review based on the requirements of your country or institution) were obtained?

Answer: [N/A]

Justification: This is not human-subjects research; it analyzes Venus cloud-top imagery, so IRB approval/waiver is not applicable.